Bone Generation Profiling Around Photofunctionalized Titanium Mesh

Makoto Hirota, DDS, PhD[1]/Takayuki Ikeda, DDS, PhD[1]/Masako Tabuchi, DDS, PhD[1]/
Kaori Nakagawa, DDS[1]/Wonhee Park, DDS, PhD[1]/Manabu Ishijima, DDS, PhD[1]/
Naoki Tsukimura, DDS, PhD[2]/Yoshiyuki Hagiwara, DDS, PhD[3]/Takahiro Ogawa, DDS, PhD[4]

Purpose: *The aim of this study was to evaluate whether photofunctionalization of titanium mesh enhances its osteoconductive capability.* ***Materials and Methods:*** *The titanium mesh (0.2 mm thickness) used in this study was made of commercially pure grade-2 titanium and had hexagonal apertures (2 mm width). Photofunctionalization was performed by treating titanium mesh with UV light for 12 minutes using a photo device immediately before use. Untreated or photofunctionalized titanium mesh was placed into rat femurs, and bone generation around titanium mesh was profiled using three-dimensional (3D) microcomputed tomography (micro-CT). A set of in vitro experiments was conducted using bone marrow–derived osteoblasts.* ***Results:*** *Photofunctionalized titanium mesh surfaces were characterized by the regenerated hydrophilicity and significantly reduced surface carbon. Bone generation profiling at week 3 of healing showed that the hexagonal apertures in photofunctionalized mesh were 95% filled, but they were only 57% filled in untreated mesh, particularly with the center zone remaining as a gap. Bone profiling in slices parallel to the titanium surface showed that photofunctionalized titanium mesh achieved 90% bone occupancy 0 to 400 μm from the surface, compared with only 35% for untreated mesh. Bone occupancy remained as high as 55% 800 to 1,200 μm from photofunctionalized titanium mesh surfaces, compared with less than 20% for untreated mesh. In vitro, photofunctionalized titanium mesh expedited and enhanced attachment and spread of osteoblasts, and increased ALP activity and the rate of mineralization.* ***Conclusion:*** *This study may provide novel and advanced metrics describing the osteoconductive property of photofunctionalized titanium mesh. Specifically, photofunctionalization not only increased the breadth, but also the 3D range, of osteoconductivity of titanium mesh, enabling space-filling and far-reaching osteoconductivity. Further translational and clinical studies are warranted to establish photofunctionalized titanium mesh as a novel clinical tool for better bone regeneration and augmentation.* Int J Oral Maxillofac Implants 2016;31:73–86. doi: 10.11607/jomi.4036

Keywords: *bone augmentation, guided bone generation (GBR), hydrophilicity, implants, osseointegration, ultraviolet (UV) light*

[1]Visiting Scholar, Weintraub Center for Reconstructive Biotechnology, UCLA School of Dentistry, Los Angeles, California, USA.
[2]Associate Professor, Department of Removable Prosthodontics, Nihon University School of Dentistry, Tokyo, Japan.
[3]Clinical Professor, Department of Fixed Prosthodontics, Nihon University School of Dentistry, Tokyo, Japan.
[4]Professor, Weintraub Center for Reconstructive Biotechnology, Division of Advanced Prosthodontics, Biomaterials and Hospital Dentistry, UCLA School of Dentistry, Los Angeles, California, USA.

Correspondence to: Dr Takahiro Ogawa, Laboratory for Bone and Implant Sciences (LBIS), Weintraub Center for Reconstructive Biotechnology, Division of Advanced Prosthodontics, Biomaterials and Hospital Dentistry, UCLA School of Dentistry, 10833 Le Conte Avenue (B3-081 CHS), Box 951668 Los Angeles, CA 90095-1668. Fax: (310) 825-6345. Email: togawa@dentistry.ucla.edu

Titanium mesh provides multiple functions, such as space-making, avoiding tissue intrusion, and/or retaining graft materials, during bone regeneration. However, its osteoconductive capability may not be utilized effectively and at least has not been explored fully for better clinical outcomes. Challenges and complications associated with the use of titanium mesh, such as exposure of titanium mesh and related infection, reduced osseointegration, longer healing time required for osseointegration, intervention of soft tissue, subsequent bone resorption, higher risk of implant failure, and esthetic problems, have been reported.[1–9] Different quality of regenerated bone compared to native bone has been evidenced in animal and human studies.[7,10–12]

Treatment of titanium implants with ultraviolet (UV) light in specific wavelengths and strengths was reported to increase the strength of bone-implant

integration more than 3 times in animal models, due to nearly complete coverage of bone around the implant.[13,14] The mechanisms underlying this improved osseointegration are the fundamentally enhanced physicochemical properties of titanium surfaces, namely, restored superhydrophilicity, decontamination of accumulated carbon, and positively converted electrostatic charge.[15,16] These factors act synergistically to increase the recruitment, attachment, and retention of osteogenic cells.[13,17–20] UV treatment is required to be undertaken immediately prior to use because these three physicochemical properties degrade substantially over time; this phenomenon is defined as biologic aging of titanium.[15,16,19,21,22] This is why UV treatment is considered as a surface conditioning rather than surface modification.[23,24] In light of these uniquely generated physicochemical functions, scientific principles, and the specific technical requirements, this surface technology is defined as photofunctionalization, differentiating itself from mere UV exposure or irradiation.

Recent studies have shown a number of data suggesting the clinical significance of photofunctionalization in accelerating the rate of implant stability development in immediate and delayed loaded implants, shortening the healing time, improving marginal bone stability, increasing the implant predictability in challenging bone conditions, and allowing for the use of shorter implants.[17,24–29] These prompted the authors of the present study to establish whether photofunctionalized titanium mesh shows better osteoconductivity than untreated, as-received titanium mesh, potentially leading to better clinical outcomes. This hypothesis was particularly challenging because of the following reasons. Previous studies on photofunctionalization used roughened titanium surfaces, such as acid-etched and sandblasted surfaces. Titanium mesh products have a relatively smooth, machined surface, which is known to delay the osteoblastic differentiation and subsequent bone formation compared to rough surfaces.[30,31] The efficacy of photofunctionalization on smooth surfaces needs to be determined. The thickness of osseointegrated bone is known to be 20 to 200 mm in rat models.[13,32] If photofunctionalization enhances bone formation only within this range, apertures within titanium mesh structure, which are much larger than 200 mm, should not be benefited by photofunctionalization. Further, the goal of titanium mesh–assisted bone augmentation should not be limited to contact osteogenesis at the mesh interface. Bone augmentation could be more effective if the thickness of de novo bone was more than 200 mm. How far the effect of photofunctionalization reaches away from titanium surfaces is of great interest. Therefore, the objective of this study was to profile bone generation around titanium mesh with or without photofunctionalization. In particular, the authors addressed the bone generation capability of titanium mesh to *(1)* fill a gap (space filling) and *(2)* extend from the surface over a distance (osteogenic reach) by establishing three-dimensional (3D) bone profiling. To confirm the results, in vitro culture studies were also conducted using bone marrow–derived osteoblasts.

MATERIALS AND METHODS

Titanium Mesh Surface Characterization and Photofunctionalization

The titanium mesh (0.2 mm thickness), made of commercially pure grade-2 titanium (KLM Martin), was trimmed to fit either 12- or 24-well culture dishes for in vitro studies or cut to 3 × 10 mm for in vivo studies. Titanium mesh contained hexagonal apertures (2 mm width) within a titanium frame (0.5 mm width), with a calculated aperture ratio of 54.7%. The surface morphology and chemistry was examined using scanning electron microscopy (SEM) (XL30, Philips, Eindhoven, Netherlands) and energy dispersive x-ray spectroscopy (EDX), respectively. The hydrophilic and hydrophobic properties of titanium mesh surfaces were evaluated by measuring the contact angle of 10 μL of H_2O. The contact angle was measured on the side-view photographic images of an H_2O droplet in triplicate as described elsewhere.[13] As described in the literature,[24–27,33] photofunctionalization was performed by treating titanium mesh with UV light for 12 minutes using a photo device (SuperOsseo, Ushio) immediately before implantation or use in cell culture. As shown in Fig 1a, titanium mesh was held on the stage placed on the drawer, and then the drawer was closed. To initiate the automated 12-minute treatment, the start button was pressed on the touch panel (Fig 1b).

Protein Adsorption

Bovine serum albumin (BSA; Pierce Biotechnology) was used as a model protein. Three hundred mL of protein solution (1 mg/mL protein/saline) was pipetted over the titanium mesh. After either 6 or 24 hours of incubation in sterile humidified conditions at 37°C, the solution containing nonadherent proteins was removed and mixed with micro bicinchoninic acid (BCA; Pierce Biotechnology) at 37°C for 60 minutes. The quantity of removed and total protein was measured using a microplate reader (Synergy HT, BioTek Instruments) at 562 nm. The rate of protein adsorption was calculated as the percentage of protein adsorbed to the titanium surfaces relative to the total amount.

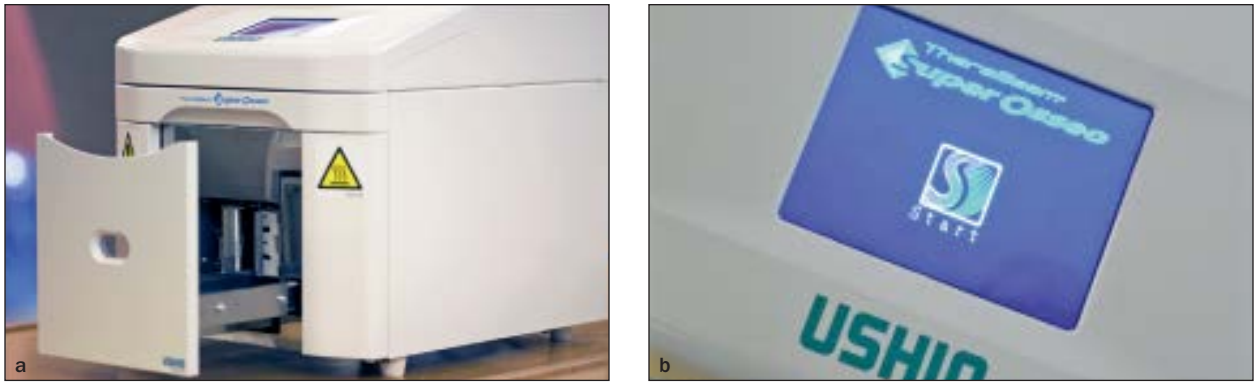

Fig 1 Photofunctionalization. *(a)* Titanium mesh held on the stage placed on the drawer of the photo device. *(b)* Touch panel to start an automated 12-minute UV treatment.

Osteoblast Cell Culture

Bone marrow cells isolated from the femurs of 8-week-old male Sprague-Dawley rats were placed into alpha-modified Eagle's medium supplemented with 15% fetal bovine serum (FBS), 50 mg/mL ascorbic acid, 10 mmol/L Na-β-glycerophosphate, 10^{-8} mol/L dexamethasone, and antibiotic-antimycotic solution. Cells were incubated in a humidified atmosphere of 95% air and 5% CO_2 at 37°C. At 80% confluency, the cells were detached using 0.25% trypsin-1 mmol/L EDTA-4Na and seeded onto titanium mesh samples at a density of 4×10^4 cells/cm^2. The culture medium was renewed every 3 days.

Cell Attachment Assay

The attachment of cells was evaluated by measuring the number of cells attached to titanium mesh samples after 6 and 24 hours of incubation using WST-1-based colorimetry (WST-1, Roche Applied Science). The culture well was incubated with 100 mL tetrazolium salt (WST-1) reagent at 37°C for 4 hours. The amount of formazan produced was measured using an ELISA reader at 420 nm.

Morphology and Spreading Behavior of Osteoblasts

Confocal laser scanning microscopy was used to assess spreading behavior and cytoskeletal arrangement of osteoblasts seeded onto titanium mesh surfaces. Three and 24 hours after seeding, cells were fixed in 10% formalin and stained using rhodamine phalloidin fluorescent dye (actin filament, red color; Molecular Probes). Cells were additionally stained with mouse anti-vinculin monoclonal antibody (Abcam), followed by fluorescein isothiocyanate (FITC)-conjugated anti-mouse secondary antibody (Abcam), to visualize intracellular expression and localization of vinculin, a focal adhesion protein. The area, perimeter, Feret's diameter, and intensity of actin and vinculin expression per cell were quantified using image analysis software (ImageJ, NIH).

Cell Density and Proliferation Assays

Propagated cells were quantified as cell density at day 4 of culture. Quantification was performed using WST-1–based colorimetry as described earlier. In addition, proliferation was measured by BrdU incorporation during DNA synthesis. At day 4, 100 mL of 100 mmol/L BrdU solution (Roche Applied Science) was added to the culture wells and incubated for 10 hours. After trypsinizing cells and denaturing DNA, cultures were incubated with anti-BrdU antibody conjugated with peroxidase for 90 minutes and reacted with tetramethylbenzidine for color development. Absorbance was measured using an ELISA reader at 370 nm (Synergy HT, BioTek Instruments). The obtained colorimetric value was divided by the WST-1 value to standardize relative to the amount of cells.

Alkaline Phosphatase Activity

Image- and colorimetry-based analyses were used to measure the alkaline phosphatase (ALP) activity of osteoblasts on day 7 of culture. Cells were washed twice with Hanks' solution and incubated with 120 mmol/L Tris buffer (pH 8.4) containing 0.9 mmol/L naphthol AS-MX phosphate and 1.8 mmol/L fast red TR for 30 minutes at 37°C. The ALP-positive area on photomicrographs was calculated as ([(stained area/total Ti mesh area) × 100])(%) using image analysis software (ImageJ, NIH). For a colorimetry-based assay, cultures were rinsed with ddH_2O, and 250 mL p-nitrophenylphosphate was added (LabAssay ATP, Wako Pure Chemicals) before being incubated at 37°C for 15 minutes. The ALP activity was evaluated as the quantity of nitrophenol released through the enzymatic reaction and measured at a wavelength of 405 nm using a plate reader and was divided by the WST-1 value measured on the same day to standardize the data relative to the number of cells.

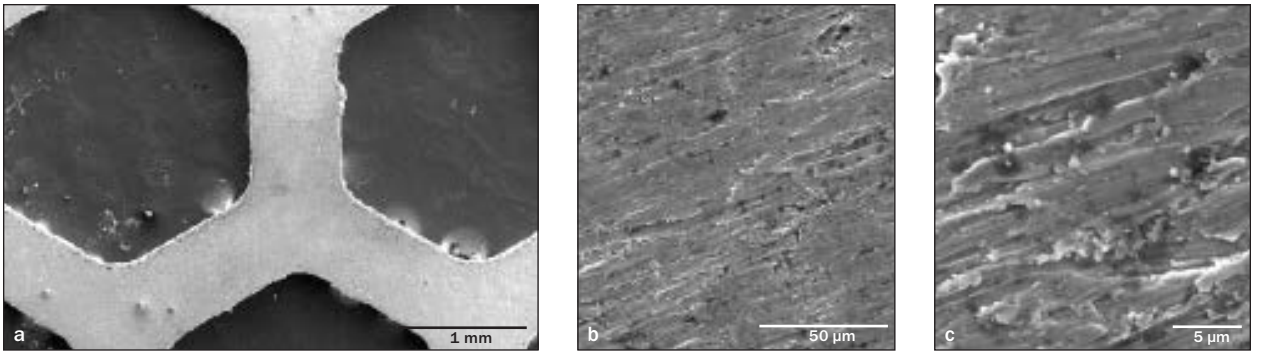

Fig 2 Surface morphology of titanium mesh used in this study. *(a, b)* Low- and *(c)* high-magnification scanning electron micrographs of the surface.

Mineralization Assay

The mineralization capability of cultured osteoblasts was examined by quantifying a mineralized nodule area and a calcium colorimetry-based assay. Mineralized nodules produced by the osteoblastic cells were visualized using the von Kossa stain. Cultures were fixed using 50% ethanol/18% formaldehyde solution for 30 minutes and incubated with 5% silver nitrate under UV light for 30 minutes before being washed twice with ddH_2O and incubated with 5% sodium thiosulfate solution for 2 to 5 minutes. The mineralized nodule area was defined as ([(stained area/total Ti mesh area) $\times$ 100]) (%) and was measured using image analysis software (Image Pro-plus, Media Cybernetics). For colorimetric detection of calcium deposition, cultures were washed with phosphate buffered saline (PBS) and incubated overnight in 1 mL of 0.5 mol/L HCl solution with gentle shaking. The solution was mixed with o-cresolphthalein complexone in alkaline medium (Calcium Binding and Buffer Reagent, Sigma) to produce a red calcium-cresolphthalein complexone complex. Color intensity was measured using a plate reader (Synergy HT, BioTek Instruments) at 575 nm. The obtained colorimetric value was divided by the WST-1 value measured on the same day to standardize the data relative to the amount of cells.

Surgery

Rats were anesthetized by inhalation with 1% to 2% isoflurane. After their legs were shaved and scrubbed with 10% providone-iodine solution, the distal aspects of the femurs were carefully exposed via a skin incision and muscle separation. The flat surfaces of the distal femurs were selected for titanium mesh placement. The site was prepared 16 mm from the distal edge of the femur by drilling a rectangular osteotomy (0.25 $\times$ 10 mm) along the longitudinal axis of the femur using a bur and scalpel. Untreated or photofunctionalized titanium mesh was placed into the femur with passive retention. Muscle and skin were sutured separately with resorbable suture thread. The protocol was approved by the Chancellor's Animal Research Committee at the University of California at Los Angeles (UCLA), and all experimentation was performed in accordance with the United States Department of Agriculture (USDA) guidelines on animal research.

In Vivo ALP Activity

At day 5 of healing, animals were sacrificed, and titanium mesh with adherent tissue was extracted for assessment of ALP activity. Of the four hexagonal apertures, three were used for ALP colorimetric detection, and the remaining aperture was used for image-based detection using the protocols described earlier.

Morphologic and Elemental Analyses of the Tissue/Ti Mesh Complex In Vivo

At weeks 2 and 3 of healing, titanium mesh samples were carefully retrieved from the rat femurs, soaked in agitated water for 1 hour, and dried under heat and vacuum. After being carbon sputter-coated, the specimens were examined by SEM. The elemental composition of the covering tissues was analyzed by energy dispersive x-ray spectroscopy (EDX). The EDX device equipped with SEM was used to detect Ti, Ca, and P elemental signals and atomic percentages within the titanium mesh and tissue complex. Elemental mapping along with the intensity spectra were used to locate and measure the intensity of the three elements. To examine the quality of tissue mineralization, Ca/P atomic ratio was evaluated. These analyses were conducted at nine randomly selected areas per specimen.

Bone Generation Profiling Using Microcomputed Tomography

The method used for the assessment of bone formation around titanium has previously been validated and is described elsewhere.[34,35] Briefly, titanium mesh/tissue specimens fixed in 10% buffered formalin were scanned using a desktop microcomputed tomography

(micro-CT) machine (mCT 40, SancroMedica) with an isotropic resolution of 8 mm. Approximately 1,250 and 300 CT slices were imaged along the longitudinal axis of and in parallel with the Ti mesh, respectively, at a radiographic energy level of 70 kVp with a current of 114 mA. Grayscale images were processed using a Gaussian low-pass noise filter and threshold algorithms to distinguish titanium and mineralized bone from background. The specific thresholds for titanium and bone tissue were determined by imaging the original materials. In order to map the bone generation profile around the titanium, bone occupancy (%) was analyzed by segmenting the surrounding tissues into two different zones or layers. To measure space-filling, the titanium mesh hexagonal aperture was divided into five 200-mm concentric zones with level 1 being next to the titanium frame edge and level 5 being the farthest away in the center of the aperture. To assess osteogenic reach, three layers, each 400 mm thick, were segmented parallel to the surface of the titanium mesh and extending 1,200 mm from the surface.

Statistical Analysis

All in vitro culture studies including the hydrophilicity test were performed in triplicate (n = 3), except for cell morphometry (n = 6). In vivo ALP analysis and bone morphometry were performed in four rats for each of weeks 2 and 3 (n = 4). For in vivo elemental analysis of the tissue, nine areas were evaluated within the specimen, and the average values were used for statistical analysis. A *t* test was used to examine differences between untreated and photofunctionalized groups after confirming the normal distribution in each of the groups; $P < .05$ was considered statistically significant.

RESULTS

Surface Morphology of Titanium Mesh

Low-magnification SEM showed that titanium mesh has a smooth surface morphology (Figs 2a and 2b). High-magnification images showed irregularly roughened features consisting of parallel-marked, scraping, and scratching traces at the supramicron level, similar to those typically seen on machined titanium surfaces (Fig 2c).

Surface Property Changes After Photofunctionalization

Untreated titanium mesh surfaces were hydrophobic, with a 10-mL H_2O drop placed on the surface remaining in droplet form without spreading and a contact angle of H_2O of approximately 90 degrees (Fig 3a). Titanium mesh surfaces were superhydrophilic after photofunctionalization, with an H_2O drop immediately spreading onto a large area of the surface with a contact angle of 0.0 degrees (Fig 3a). As expected, only Ti and C were detected on Ti mesh surfaces using EDX elemental analysis. A significant reduction in carbon signal was noted on the photofunctionalized surfaces (Fig 3b), with the atomic percentage of carbon reducing from 15% to 8% after photofunctionalization.

Protein Adsorption and Initial Cell Attachment and Behavior

The amount of albumin adsorbed onto titanium mesh during a 6-hour period of incubation was 2.5 times greater on photofunctionalized than untreated surfaces (Fig 4a). The difference remained significant even after 24 hours. Similarly, the number of osteoblasts attaching during 6 and 24 hours of incubation approximately doubled on photofunctionalized surfaces, which was visually confirmed using confocal microscopy (Fig 4b).

Confocal microscopy of osteoblasts dual-stained with rhodamine phalloidin and anti-vinculin antibodies showed that the cells were apparently larger on photofunctionalized titanium mesh than on untreated mesh after 3 hours of incubation (Fig 5a to 5d). Cells attached to photofunctionalized surfaces had a stretched morphology with clear lamellipodia-like cytoplasmic projections and development of cytoskeletal fibers within their cytoplasm, whereas a majority of cells on untreated surfaces remained circular at 3 hours and only rarely showed features of cytoplasmic elongation or cytoskeletal development. After 24 hours of incubation, the cells spread on both surfaces, with those on photofunctionalized surfaces even larger than those on untreated surfaces with well-formed and extensive actin fiber formation and prominent cellular projections. Anti-vinculin staining alone demonstrated that the entire cytoplasm was vinculin-positive on photofunctionalized surfaces, with particularly intensive localization at the tips of cytoplasmic projections (Fig 5e to 5h).

Cytomorphometric analysis of cell area, perimeter, and Feret's diameter showed significant differences between untreated and photofunctionalized titanium mesh surfaces, consistent with the qualitative observations (Fig 5i). Densitometric analysis for actin and vinculin expression also confirmed that there was significantly upregulated expression of these molecules on photofunctionalized surfaces (Fig 5i).

Cell Proliferation and Functional Phenotypes

The cell density was significantly greater on photofunctionalized titanium mesh on day 4 of culture than on untreated controls (Fig 6, left). The rate of BrdU

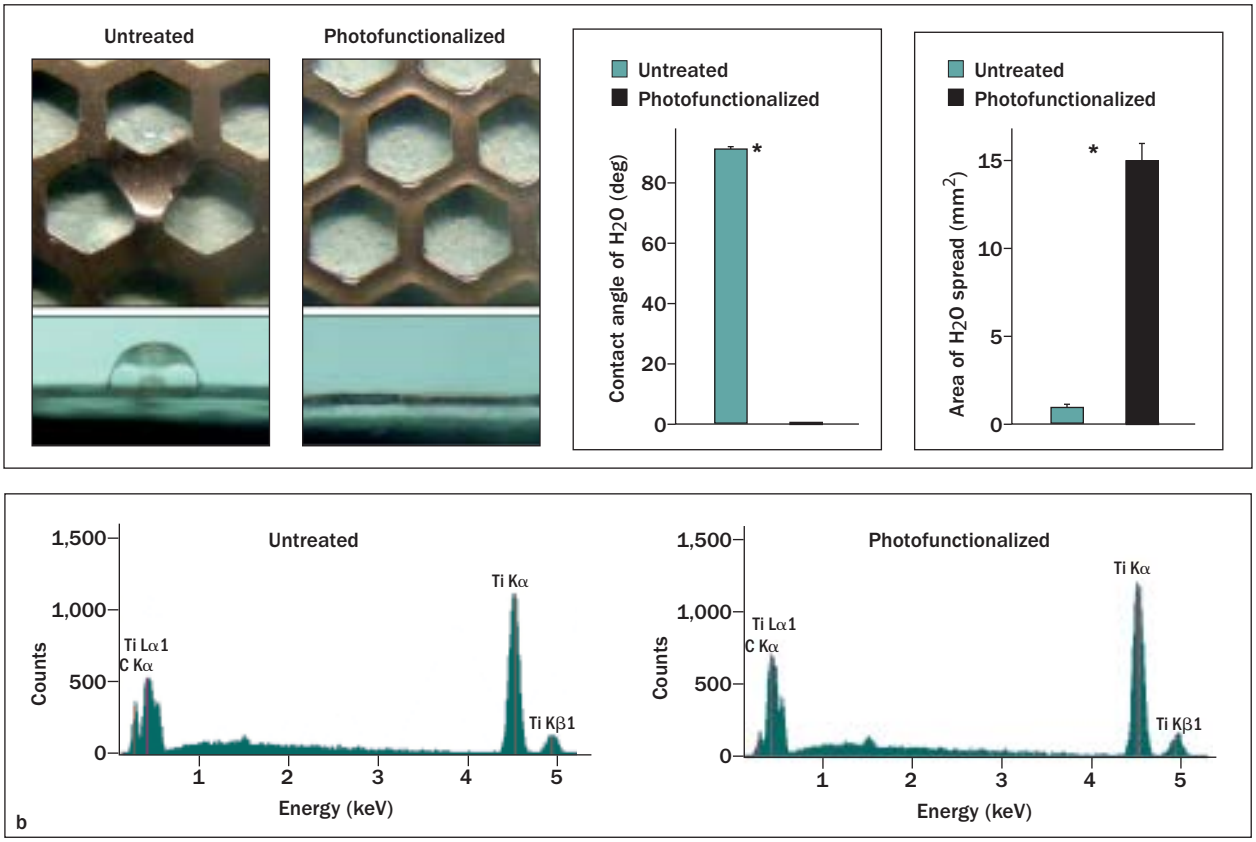

Fig 3 Surface property changes of titanium mesh before and after photofunctionalization. *(a)* Change from hydrophobic to superhydrophilic surfaces by photofunctionalization. Top and side views of 10 mL ddH_2O placed on titanium mesh as well as the contact angle. Data are means ± SD (n = 3). *P < .001, indicating a statistically significant difference between untreated and photofunctionalized surfaces. *(b)* Energy dispersive x-ray spectroscopic (EDX) spectrum of the surface before and after photofunctionalization.

Fig 4 Protein adsorption and cellular attachment to titanium mesh. *(a)* The amount of albumin adsorbed to titanium mesh with or without photofunctionalization after 6- and 24-hour incubation. *(b)* The number of attached cells during 6- and 24-hour incubation evaluated by WST-1 assay. Confocal microscopic images of osteoblasts after a 6-hour incubation are also shown. Data are means ± SD (n = 3). *P < .05; **P < .01, indicating a statistically significant difference between untreated and photofunctionalized surfaces.

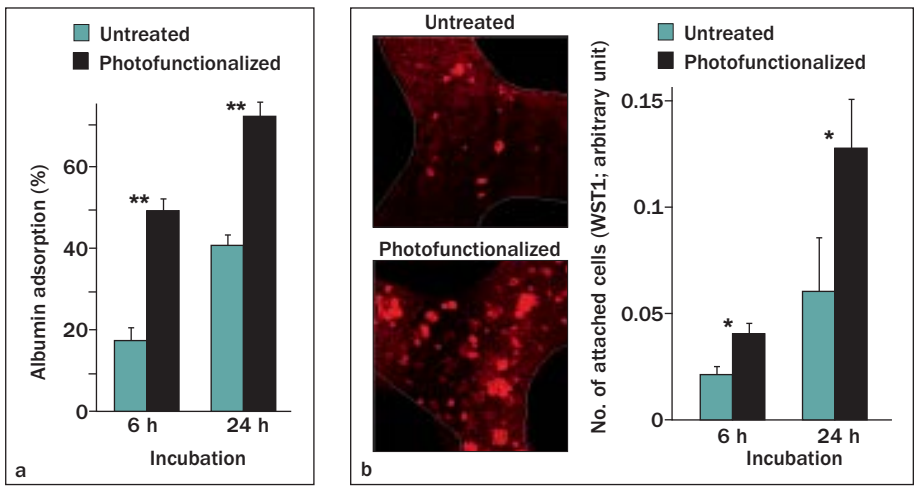

incorporation into DNA normalized by the amount of cells measured on day 4 was also significantly greater on photofunctionalized surfaces (Fig 6, right), suggesting that the increase in cell density was due to the increased number of attached cells within 24 hours and subsequent cellular proliferation.

Day 7 ALP activity, measured using image-based densitometry on photofunctionalized surfaces, was approximately twice that of untreated surfaces (Fig 7a). The ALP activity colorimetrically measured and standardized by the amount of cells was also increased (Fig 7b). The area of mineralized nodules visualized with von Kossa staining was significantly increased on photofunctionalized surfaces (Fig 7c), and calcium deposition colorimetrically evaluated and standardized by the amount of cells was also increased (Fig 7d).

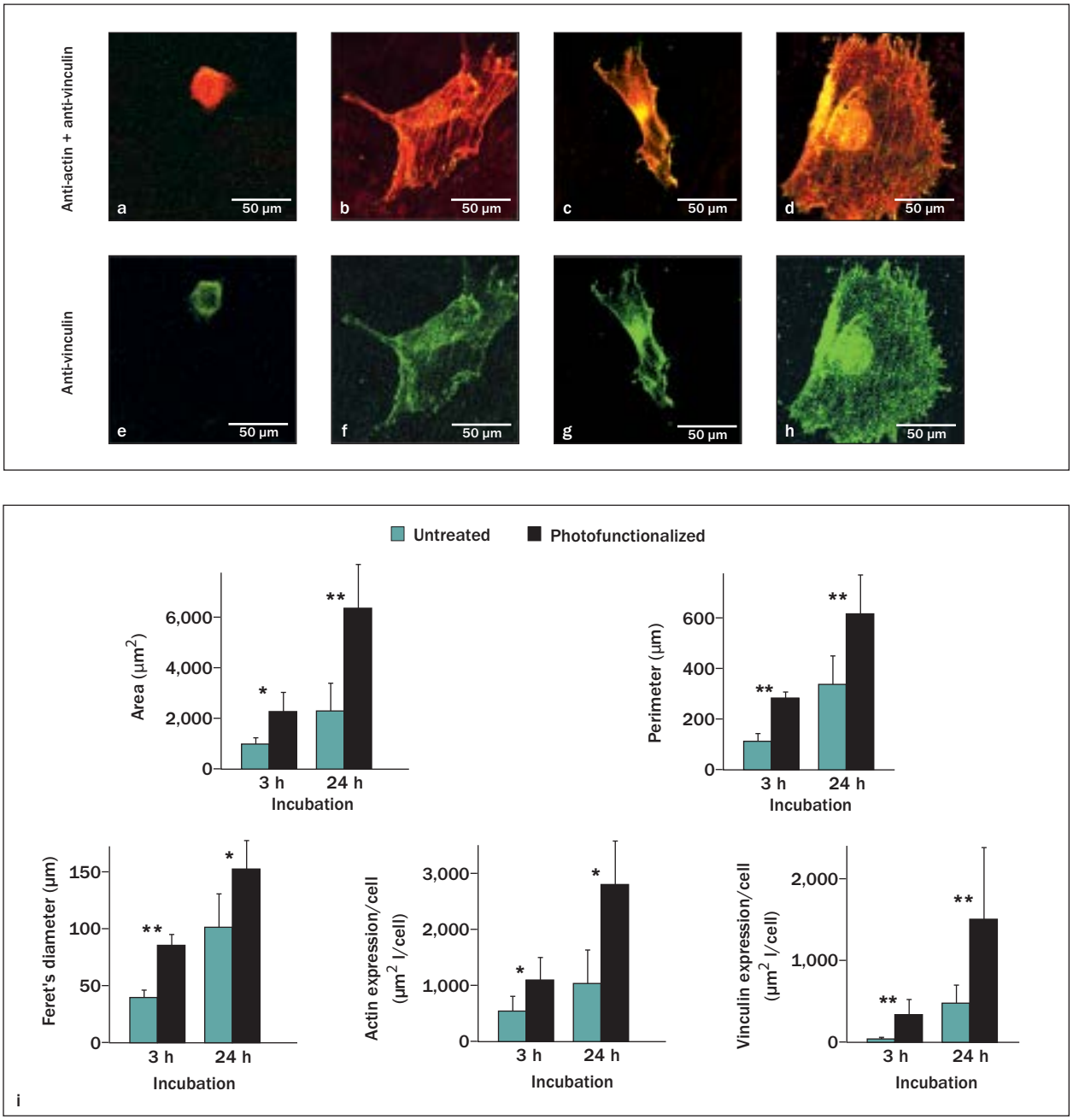

Fig 5 Initial attachment and spreading behavior of osteoblasts on *(a, c, e, g)* untreated and *(b, d, f, h)* photofunctionalized titanium mesh surfaces *(a, b, e, f)* 3 and *(c, d, g, h)* 24 hours after seeding. *(a to h)* Confocal microscopic images of osteoblasts with immunochemical stain for cytoskeletal actin and adhesion protein vinculin. *(i)* Cytomorphometric and densitometric parameters measured from the images. Data are means ± SD (n = 6). **P* < .05; ***P* < .01, indicating a statistically significant difference between untreated and photofunctionalized surfaces.

In Vivo Osteogenic Activity and Bone Morphology Around Titanium Mesh

Titanium mesh placed into rat femurs was retrieved at day 5 of healing (top image, Fig 8a) and subjected to ALP staining (bottom image, Fig 8a) and colorimetric detection (Fig 8b). Both assays showed that ALP activity was greater in the tissue around the photofunctionalized titanium mesh than untreated controls.

Tissue that formed around titanium mesh was morphologically and elementally examined using SEM and EDX, respectively. De novo tissue formation appeared to be more extensive around the photofunctionalized titanium mesh at week 2 of healing (Fig 9a). SEM images show that all apertures were clearly recognizable on untreated titanium mesh. Fragmented and discrete formation of tissue was observed on untreated

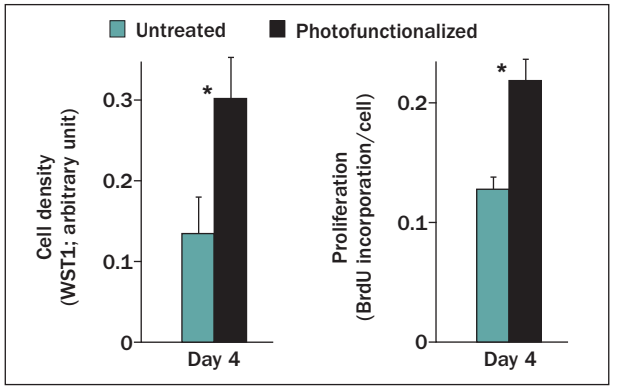

Fig 6 Cell density and proliferative activity of osteoblasts cultured on untreated and photofunctionalized titanium mesh on day 4 of culture. Data are means ± SD (n = 3). *$P < .05$, indicating a statistically significant difference between untreated and photofunctionalized surfaces.

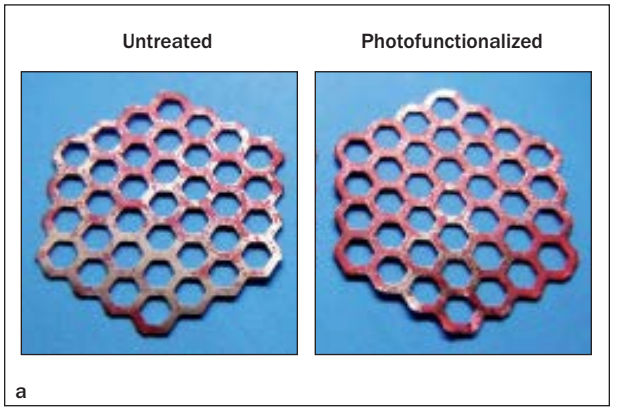

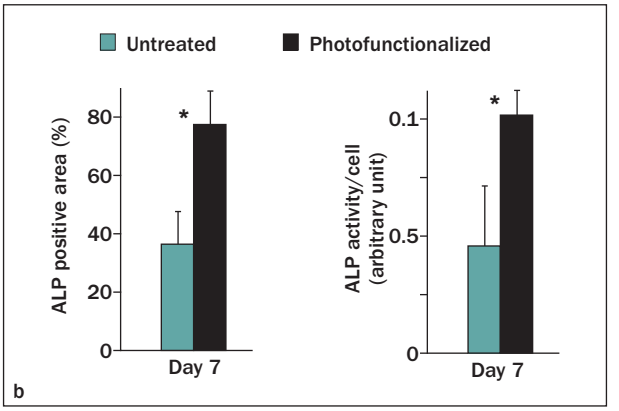

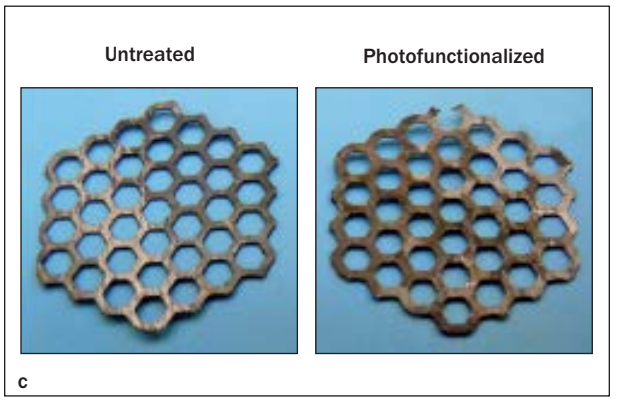

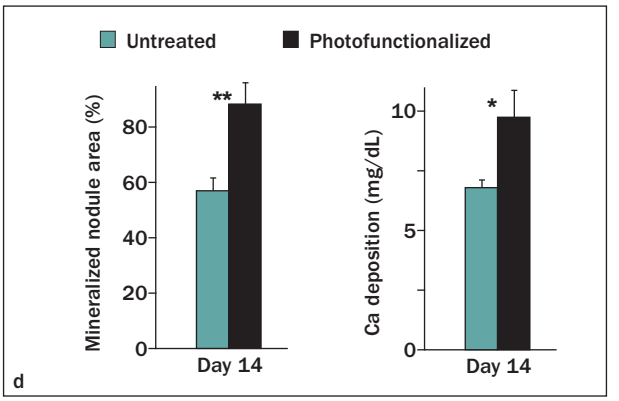

Fig 7 Osteoblastic functional phenotypes on Ti mesh. *(a)* Culture images at day 7 after alkaline phosphatase (ALP) stain and a histogram of the calculated ALP positive area (%). *(b)* Colorimetric assay was also performed for ALP activity. *(c)* Osteoblastic cultures at day 14 after von Kossa stain along with the densitometrically calculated mineralized nodule area (%). *(d)* The amount of calcium deposition colorimetrically measured on the same day of culture. Data are means ± SD (n = 3). *$P < .05$; **$P < .01$, indicating a statistically significant difference between untreated and photofunctionalized surfaces.

titanium mesh surfaces, but a majority of bare titanium surface was exposed with little biologic structure as seen at higher magnification (top left image, Fig 9). In contrast, most of the aperture and titanium frame were covered and obscured by newly formed tissue on photofunctionalized mesh (Fig 9a).

By week 3 of healing, tissue formation around photofunctionalized titanium mesh was even more extensive and had a thick and dense appearance. Approximately half of the untreated titanium mesh was covered by new tissue. EDX analysis showed that the newly formed tissue contained prominent Ca and P signals with only a faint Ti peak, regardless of tissues on untreated and photofunctionalized mesh, indicating that those tissues were mineralized bone (Fig 9b). The Ca/P ratio was not significantly different between the bone tissues on untreated and photofunctionalized titanium mesh at weeks 2 and 3 (Fig 9c), indicating that the degree of mineralization was comparable between the two surfaces.

3D Bone Profiling Within Mesh Apertures

A large proportion of apertures in photofunctionalized titanium mesh were filled with bone at week 2 of healing in CT images (Fig 10a), with bone formation expanding even to the central area of the aperture. In contrast, formation of new bone was limited and confined to areas adjacent to the titanium frame edge in untreated titanium mesh. By week 3, bone formation advanced further in both photofunctionalized and untreated specimens. Almost the entire aperture was filled with bone in photofunctionalized titanium mesh, whereas there was still an absence of bone in the center of the aperture in untreated mesh. Bone morphometry demonstrated that bone volume within the aperture was increased by 180% and 60% by photofunctionalization at weeks 2 and 3, respectively (Fig 10b). The bone occupancy within the aperture of photofunctionalized titanium mesh was approximately 95% compared to 57% for untreated titanium mesh at week 3.

Further bone morphometry was conducted to profile the pattern of osteogenesis within the aperture. A single aperture was segmented into five zones from the titanium edge to the center (left panel, Fig 10c), and bone volume as measured by occupancy percent was plotted for each segment (line graphs, Fig 10d). At week 2, the bone occupancy was approximately 65% in the outermost segment (0- to 200-mm zone), which was maintained at relatively high levels (35% to 40%) into the central segment (800- to 1,000-mm zone, furthest from the titanium edge) for the photofunctionalized mesh. The untreated mesh had considerably lower bone occupancy, starting at approximately 20% in the outermost segment and dropping to less than 5% in segments 3 to 5 (400 mm and beyond). At week 3, the bone occupancy was approximately 90% in the outermost segment of photofunctionalized mesh, and this was maintained at 70% or higher in the central zone. In comparison, bone occupancy in untreated mesh started at 60% and rapidly dropped as the distance increased from the edge (to < 30% bone occupancy in zones 4 and 5).

3D Bone Profiling in Different Layers

Representative 3D CT images are presented to visualize osteogenesis stemming at the titanium mesh surface to the level 1.2 mm distance from the surface (Fig 11a). Both at weeks 2 and 4, bone appeared to be denser around photofunctionalized Ti mesh. Total bone occupancy within the 1.2-mm adjacent zone was approximately 2 times higher for photofunctionalized mesh than for the untreated one at week 2, and the difference remained significant at week 3 (Fig 11b).

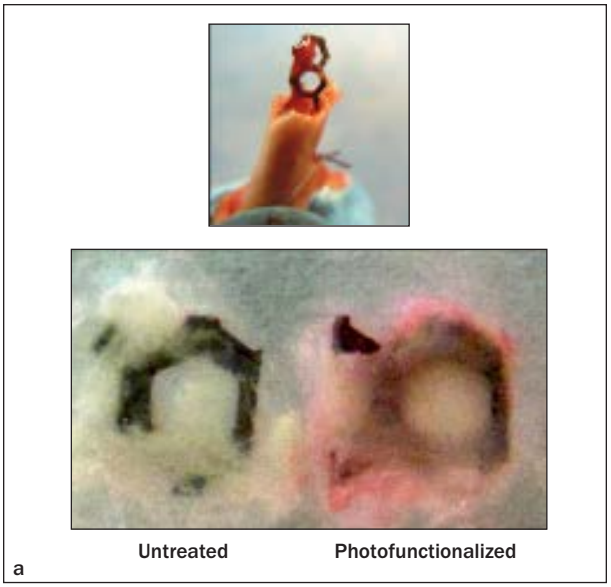

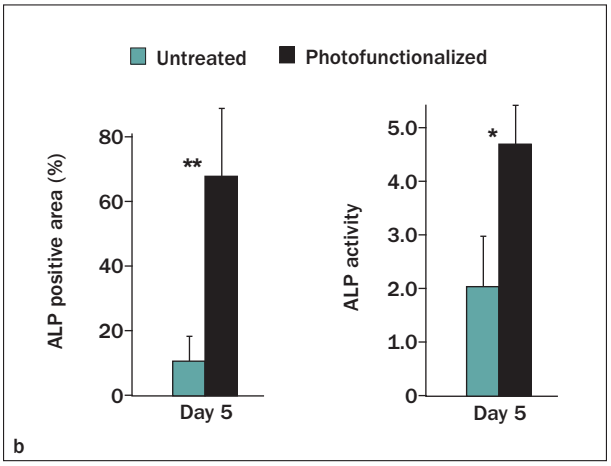

Fig 8 In vivo ALP activity in tissues around titanium mesh with and without photofunctionalization. *(a)* Ti mesh samples were retrieved from the femur at day 5 of healing *(top)* and stained for ALP activity *(bottom right).* ALP positive area (%) was measured on these stained images. *(b)* ALP activity colorimetrically measured is also shown for confirmation. Data are means ± SD (n = 3). **P* < .05; ***P* < .01, indicating a statistically significant difference between untreated and photofunctionalized surfaces.

Bone generation was profiled by plotting the bone occupancy in each of the layers (1 to 3) from the titanium mesh surface (left image, Fig 11c). At week 2, the bone occupancy was greater than 65% for photofunctionalized titanium mesh in the adjacent area (layer 1), but was less than 30% in untreated titanium mesh. Bone occupancy decreased in more distant layers in both mesh groups, but photofunctionalized mesh occupancy remained significantly greater throughout the layers. At week 3, bone occupancy for photofunctionalized titanium mesh was 90% in layer 1 and 55% in layer 3. In contrast, the bone occupancy of untreated mesh was lower than 40% regardless of the layers and did not significantly increase between weeks 2 and 3.

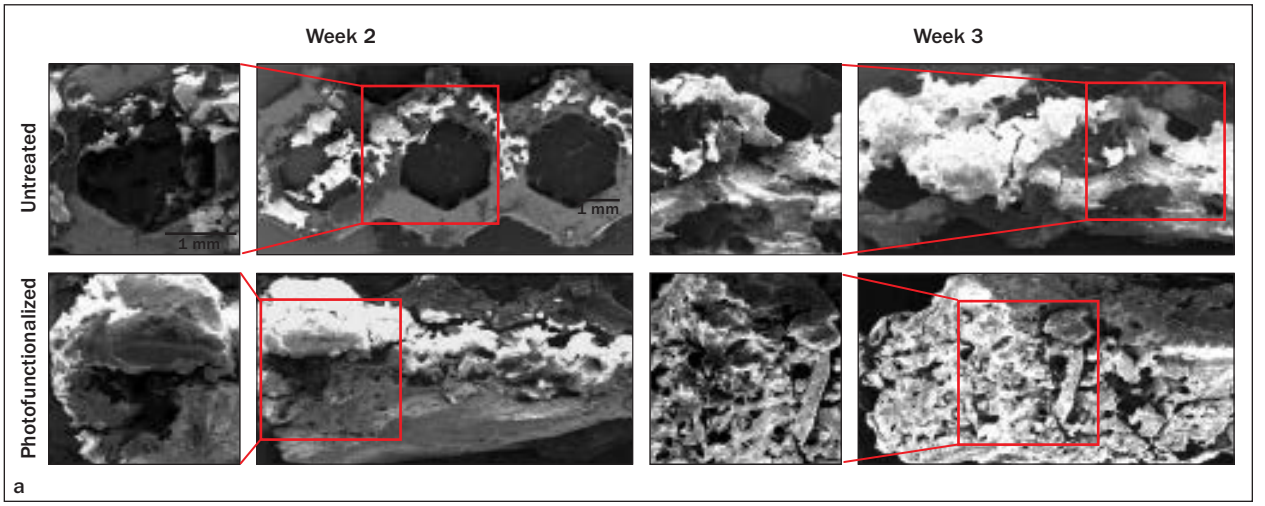

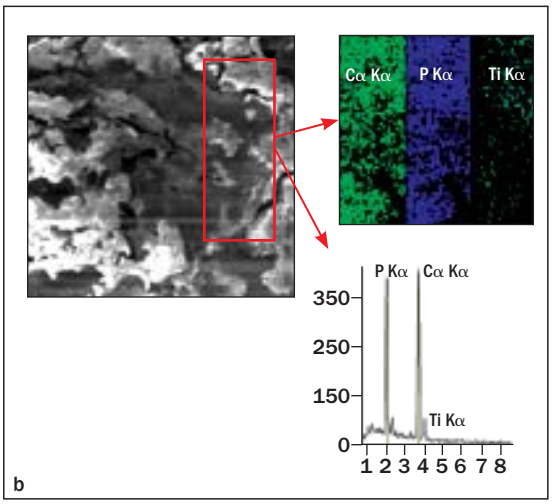

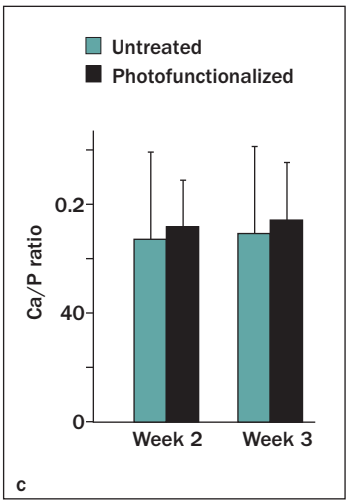

Fig 9 Morphology and chemistry of tissues formed in vivo around titanium mesh with and without photofunctionalization. *(a)* Scanning electron micrographs (SEM) of the titanium mesh retrieved at weeks 2 and 3 of healing. Magnified images from each of the red squares are also presented. *(b)* A representative EDX mapping for the tissue around titanium mesh. *(c)* Tallied Ca/P ratio. Data are means ± SD (n = 4).

DISCUSSION

Here the authors described the 3D osteoconductivity of photofunctionalized titanium mesh and demonstrated its enhanced capability to fill a defined space and extend from the surface. Specifically, osteoconductivity was enhanced by photofunctionalization to the extent that the bone occupancy of the 2 × 2-mm mesh aperture reached 95% by week 3 of healing in an animal model. This was in contrast to 57% bone occupancy for untreated mesh after the same healing time. The difference between the two groups was even greater at early healing (week 2), with bone occupancy of greater than 60% for photofunctionalized mesh, which was 2.5 times greater than untreated controls.

With regards to osteoconductivity reach, the authors postulate that this is a unique property of titanium, distinct from the commonly evaluated parameters for osteoconductivity that focus on the breadth of bone formation, such as the percentage of bone-titanium contact. The authors therefore assessed the extent of bone formation extending outward in layers from the titanium mesh surface. Photofunctionalized titanium mesh not only increased bone occupancy to 90% at the layer nearest the surface, but also induced a bone occupancy as high as 55% 1.2 mm from the titanium surface, which was more than 2.5 times greater than untreated titanium surfaces. These results reveal a novel advantage of photofunctionalized titanium, namely, far-reaching osteoconductivity, in addition to the well-established phenomenon of high bone-titanium contact.

Photofunctionalized titanium mesh expedited and enhanced cell attachment and spread, which are assumed to have contributed to the enhancement of peri-titanium osteogenesis. One of the questions addressed in this study was whether photofunctionalization was effective on machined surfaces as mentioned in the Introduction. In addition to the increased proliferation, ALP activity and Ca deposition standardized by the quantity of cells were increased, indicating that cellular differentiation was also increased on photofunctionalized titanium mesh. Increased cellular interaction by the increased cell density may have caused

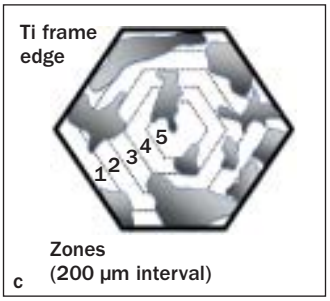

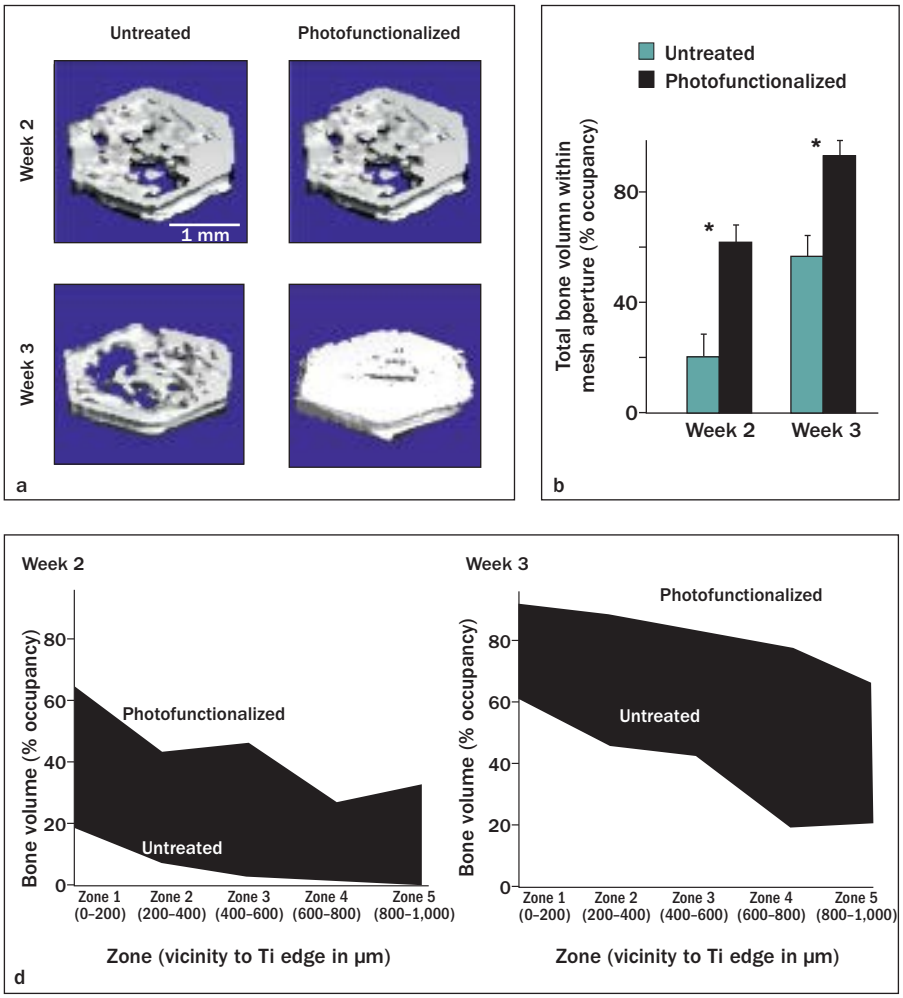

Fig 10 Bone generation profiling and morphometry performed at weeks 2 and 3 of healing within the apertures of titanium mesh. *(a)* Representative micro-CT images of bone formed within a hexagonal aperture of untreated and photofunctionalized titanium mesh. *(b)* Total bone volume within a titanium mesh aperture evaluated as the bone occupancy percentage using micro-CT morphometry. Data are means ± SD (n = 4). *P < .05, indicating a statistically significant difference between untreated and photofunctionalized titanium mesh. *(c)* Micro-CT–based bone generation profiling along the vicinity level to the edge of the titanium mesh from the closest zone (zone 1) to the farthest/central zone (zone 5) as shown in the left diagram. *(d)* The mean bone volume in each of the zones as bone occupancy percent is plotted in the line graphs at weeks 2 and 3 of healing (n = 4).

the increased differentiation. The detailed mechanism needs further studies. Importantly, these in vitro phenomena comprehensively explained the increased breadth of osteoconductivity acquired on the photofunctionalized titanium surface, but only indirectly explained far-reaching osteoconductivity. One possibility to explain the enhanced reach might be that it is due to not only the increased number of attached cells, but also the enhanced retention of cells on photofunctionalized titanium mesh surfaces. In support of this, vinculin (an adhesion molecule) was highly expressed in cells growing on photofunctionalized mesh. Enhanced cellular retention might allow for layered cell attachment in vivo, resulting in thicker bone formation. Another hypothesis is that photofunctionalization-enhanced protein adsorption further increases cell attachment in vivo. As demonstrated here, albumin adsorption was increased on photofunctionalized mesh. While in vitro there is only a single source of seeded cells, in vivo there is a constant cellular supply, and the enhanced adsorption of proteins may have resulted in layered cell attachment. Finally, the physicochemical changes induced by photofunctionalization, ie, the conversion from electronegative to electropositive, may have caused an increase in cellular recruitment in vivo. Cells are negatively charged, and therefore, there is little direct interaction between cells and the conventional titanium surface, which is a reason why titanium is referred to as bioinert.[36,37] In contrast, photofunctionalized titanium, which is electropositive, enables the direct interaction of titanium with cells and accelerates and enhances cell recruitment and attachment.

The validity of micro-CT to evaluate the bone formation around titanium was examined in a previous study from the present authors.[34] When used in the rat femur model, there was a significant correlation between the results of histology and micro-CT in the peri-implant tissue at 24 mm or more distant, demonstrating the reliability of micro-CT data. Based on this, the authors segmented the peri-implant tissue into the zones, where the closest zone to the mesh surface was much larger than 24 mm, ie, 0 to 200 mm in the aperture analysis and 0 to 400 mm in the osteogenic

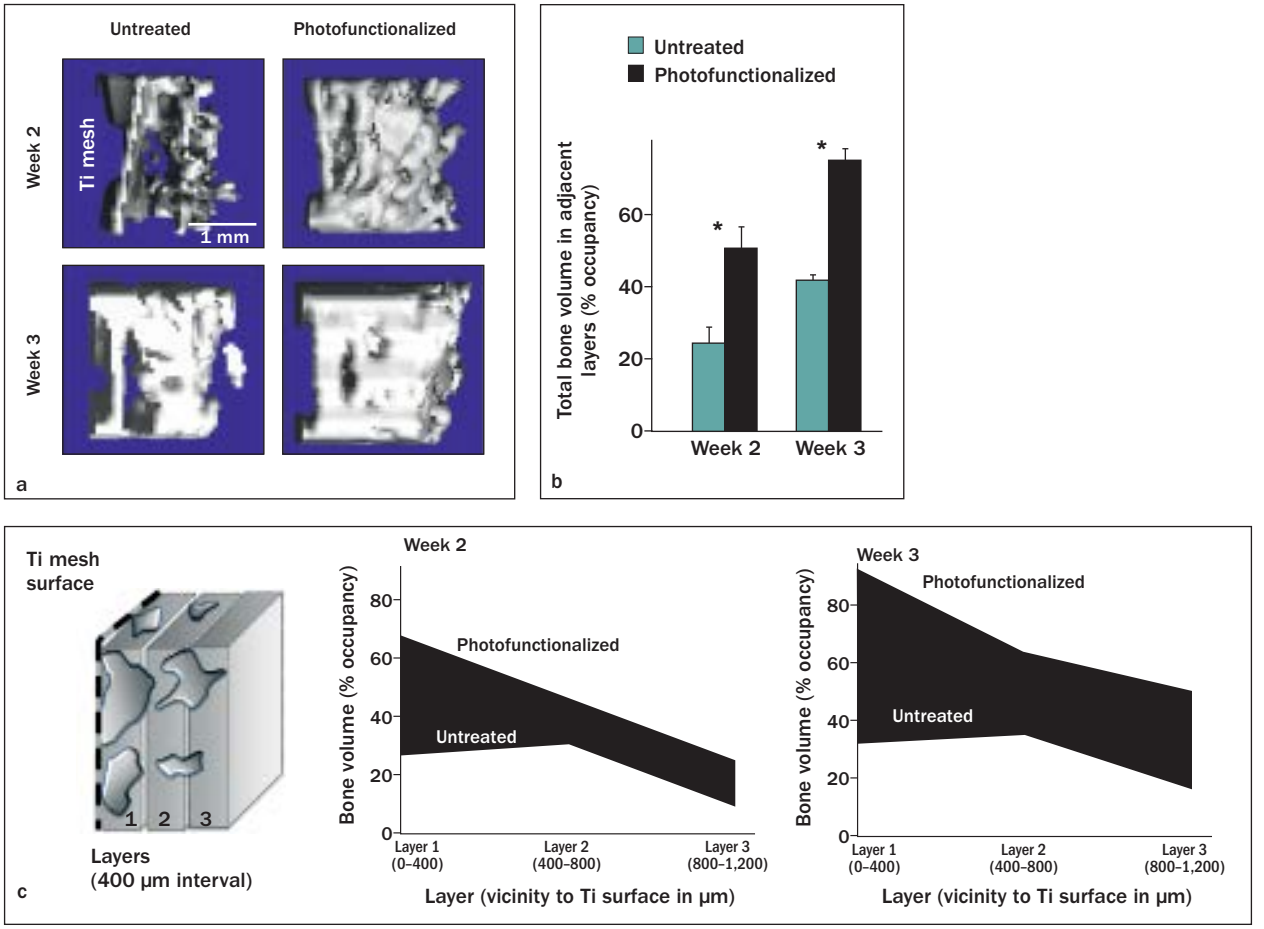

Fig 11 Bone generation profiling and morphometry performed at weeks 2 and 3 of healing in the adjacent zone from the titanium mesh surface. *(a)* Representative micro-CT images of bone formed around untreated and photofunctionalized titanium mesh. Titanium mesh is located at left side in each panel. *(b)* Total bone volume as the bone occupancy percent formed within the 1.2-mm adjacent zone to the titanium mesh surface. Data are means ± SD (n = 4). *$P < .05$, indicating a statistically significant difference between untreated and photofunctionalized titanium mesh. *(c)* Micro-CT–based bone generation profiling along the vicinity level to the surface of the titanium mesh from the closest/interfacial layer (layer 1) to the furthest layer (layer 3) as shown in the left diagram. The mean bone volume in each of the layers as bone occupancy percent is plotted in the line graphs at weeks 2 and 3 of healing (n = 4).

reach analysis, thus minimizing the possible artifact by titanium. The authors believe the micro-CT analysis outside these closest zones was little affected by the presence of titanium. Nonetheless, the use of histology to support the micro-CT results was considered in the current study. However, tissue specimens containing a titanium mesh with a complex structure made sectioning extremely difficult. The mesh surface without roughening does not retain the tissue and increases the difficulty. Moreover, a major purpose of this study was to examine the space-filling capability within apertures. To obtain the image within the aperture, the specimen needed to be sectioned in parallel to the titanium mesh to a thickness much smaller than the mesh, which was nearly impossible. The authors hope future technologic advancement will overcome these methodologic problems.

The surface of the Ti mesh used in this study showed morphologic features similar to machined titanium surfaces, with no defined microroughness. As mentioned in the Introduction, osteoblastic differentiation is known to be delayed on such surfaces compared to roughened surfaces. Further, photofunctionalization increases the number of attached cells and the rate of proliferation, which might further delay the differentiation and mineralization of osteoblasts according to the known biologic principle, ie, an inverted correlation between the proliferation and differentiation.[38–41] In spite of this anticipation, the ALP activity and calcium deposition standardized by the number of cells were increased on photofunctionalized titanium mesh, suggesting that osteoblastic differentiation was not compromised and even promoted on photofunctionalized titanium mesh.

This study revealed unique features of osteoconductivity inducible on titanium and may contribute to a general field of biomaterial research beyond implant science. Previous studies on photofunctionalization

Table 1 Difference in Osteoconductive Properties Between Untreated and Photofunctionalized Titanium

			Bone generation				
	Action	Surface compatibility	Morphology	Breadth	Rate	Space-filling capacity	Osteogenic reach
Osteoconduction around untreated Ti	Passive	Bioinert	Fragmentary	Discrete	Baseline	Low	Limited to proximity
Osteoconduction around photofunctionalized Ti	Active	Bioactive	Contiguous	Extensive	Accelerated	High	Far-reaching

found that bone formation around photofunctionalized titanium implants is more complete; the pattern of bone morphogenesis was not only extensive but also contiguous.[13] This is in comparison to the bone formation seen around untreated titanium implants, with discrete formation of fragmentary bone tissues. Here the authors add the features of space-filling and far-reaching osteoconductivity of photofunctionalized titanium, which until now the bone morphogenetic parameters could not isolate or identify. As mentioned earlier, the bone morphogenesis around photofunctionalized titanium is based on a newly rendered positive interaction between titanium and cells, as opposed to the osseointegration occurring around inert as-received titanium. The authors therefore postulate that osteoconduction around photofunctionalized titanium is an active process (Table 1).

The present results indicate that photofunctionalization may increase the value of the use of titanium mesh. Whether titanium mesh is used as a permanent implant device as in the fixation of fractured bone or a temporary device for preimplant bone augmentation, the accelerated and enhanced osteoconductivity induced by photofunctionalization is expected to have a positive clinical impact. If photofunctionalized titanium mesh is able to generate a greater quantity of bone in a shorter period of time, it would have an impact on clinical demands of faster healing and stronger foundation of bone. Future clinical studies would be particularly important to address the potential improvement in speed, quantity, and quality of bone regeneration using photofunctionalized titanium mesh. In the current study, the variation of effects, as represented by the standard deviation, ranging from 5% to 20% for in vitro studies and from 10% to 30% for in vivo studies was relatively small, suggesting consistency in the animal model. Future translational and clinical studies are required to examine the efficacy of photofunctionalization under various local and systemic conditions, such as different regions in the jawbone and bone under osteoporotic, diabetic, aging, and other challenging conditions.

CONCLUSIONS

In this study, the authors conducted 3D profiling of bone generation around photofunctionalized titanium mesh. In an in vivo model of osteogenesis, hexagonal apertures measuring 2 × 2 mm in photofunctionalized titanium mesh were 95% filled at week 3 of healing but only 57% filled if untreated. Photofunctionalized titanium mesh induced 90% bone formation 0 to 400 mm from the surface, compared to only 35% for untreated mesh; bone generation was maintained at 55% for photofunctionalized mesh even 800 to 1,200 mm distance from its surface, compared to 20% for untreated controls. In vitro, photofunctionalized titanium mesh expedited and enhanced cell attachment and spread and increased the expression of osteogenic functional phenotypes, such as ALP activity and mineralization. These results comprehensively suggest that photofunctionalization enhances not only the breadth, but also the 3D range, of osteoconductivity of titanium mesh, enabling space-filling and far-reaching osteoconductivity. Further translational and clinical studies are warranted to establish photofunctionalized titanium mesh as a novel clinical tool for better bone regeneration and augmentation.

ACKNOWLEDGMENTS

This work was partially supported by a research gift from Ushio, Inc. The authors declare no conflicts of interest.

REFERENCES

1. Ishikawa T, Salama M, Funato A, et al. Three-dimensional bone and soft tissue requirements for optimizing esthetic results in compromised cases with multiple implants. Int J Periodontics Restorative Dent 2010;30:503–511.
2. Simion M, Fontana F, Rasperini G, Maiorana C. Long-term evaluation of osseointegrated implants placed in sites augmented with sinus floor elevation associated with vertical ridge augmentation: A retrospective study of 38 consecutive implants with 1- to 7-year follow-up. Int J Periodontics Restorative Dent 2004;24:208–221.

3. Urban IA, Jovanovic SA, Lozada JL. Vertical ridge augmentation using guided bone regeneration (GBR) in three clinical scenarios prior to implant placement: A retrospective study of 35 patients 12 to 72 months after loading. Int J Oral Maxillofac Implants 2009;24:502–510.
4. Chiapasco M, Casentini P, Zaniboni M. Bone augmentation procedures in implant dentistry. Int J Oral Maxillofac Implants 2009 24(suppl):237–259.
5. Santing HJ, Raghoebar GM, Vissink A, den Hartog L, Meijer HJ. Performance of the Straumann Bone Level Implant system for anterior single-tooth replacements in augmented and nonaugmented sites: A prospective cohort study with 60 consecutive patients. Clin Oral Implants Res 2013;24:941–948.
6. Funato A, Ishikawa T, Kitajima H, Yamada M, Moroi H. A novel combined surgical approach to vertical alveolar ridge augmentation with titanium mesh, resorbable membrane, and rhPDGF-BB: A retrospective consecutive case series. Int J Periodontics Restorative Dent 2013;33:437–445.
7. Miyamoto I, Funaki K, Yamauchi K, Kodama T, Takahashi T. Alveolar ridge reconstruction with titanium mesh and autogenous particulate bone graft: Computed tomography-based evaluations of augmented bone quality and quantity. Clin Implant Dent Relat Res 2012;14:304–311.
8. Roccuzzo M, Ramieri G, Bunino M, Berrone S. Autogenous bone graft alone or associated with titanium mesh for vertical alveolar ridge augmentation: A controlled clinical trial. Clin Oral Implants Res 2007;18:286–294.
9. Torres J, Tamimi F, Alkhraisat MH, et al. Platelet-rich plasma may prevent titanium-mesh exposure in alveolar ridge augmentation with anorganic bovine bone. J Clin Periodontol 2010;37:943–951.
10. Yamada Y, Sato S, Yagi H, et al. Correlation in the densities of augmented and existing bone in guided bone augmentation. Clin Oral Implants Res 2012;23:837–845.
11. Heberer S, Al-Chawaf B, Jablonski C, et al. Healing of ungrafted and grafted extraction sockets after 12 weeks: A prospective clinical study. Int J Oral Maxillofac Implants 2011;26:385–392.
12. Artzi Z, Dayan D, Alpern Y, Nemcovsky CE. Vertical ridge augmentation using xenogenic material supported by a configured titanium mesh: Clinicohistopathologic and histochemical study. Int J Oral Maxillofac Implants 2003;18:440–446.
13. Aita H, Hori N, Takeuchi M, et al. The effect of ultraviolet functionalization of titanium on integration with bone. Biomaterials 2009;30:1015–1025.
14. Att W, Hori N, Iwasa F, et al. The effect of UV-photofunctionalization on the time-related bioactivity of titanium and chromium-cobalt alloys. Biomaterials 2009;30:4268–4276.
15. Ogawa T. Ultraviolet photofunctionalization of titanium implants. Oral CraniofacTissue Eng 2012;2:151–158.
16. Att W, Ogawa T. Biological aging of implant surfaces and their restoration with ultraviolet light treatment: A novel understanding of osseointegration. Int J Oral Maxillofac Implants 2012;27:753–761.
17. Ueno T, Yamada M, Suzuki T, et al. Enhancement of bone-titanium integration profile with UV-photofunctionalized titanium in a gap healing model. Biomaterials 2010;31:1546–1557.
18. Iwasa F, Hori N, Ueno T, et al. Enhancement of osteoblast adhesion to UV-photofunctionalized titanium via an electrostatic mechanism. Biomaterials 2010;31:2717–2727.
19. Att W, Hori N, Takeuchi M, et al. Time-dependent degradation of titanium osteoconductivity: An implication of biological aging of implant materials. Biomaterials 2009;30:5352–5363.
20. Miyauchi T, Yamada M, Yamamoto A, et al. The enhanced characteristics of osteoblast adhesion to photofunctionalized nanoscale TiO2 layers on biomaterials surfaces. Biomaterials 2010;31:3827–3839.
21. Lee JH, Ogawa T. The biological aging of titanium implants. Implant Dent 2012;21:415–421.
22. Hori N, Att W, Ueno T, et al. Age-dependent degradation of the protein adsorption capacity of titanium. J Dent Res 2009;88:663–667.
23. Ishikawa T, Vela X, Kida K, et al. Restoration of optimum esthetics in complex clinical situations using an interdisciplinary strategy in combination with advanced techniques and technologies in regenerative medicine. J Cosmetic Dent 2014;29:60–72.
24. Funato A, Tonotsuka R, Murabe H, Hirota M, Ogawa T. A novel strategy for bone integration and regeneration—photofunctionalization of dental implants and Ti mesh. J Cosmetic Dent 2014;29:74–86.
25. Funato A, Yamada M, Ogawa T. Success rate, healing time, and implant stability of photofunctionalized dental implants. Int J Oral Maxillofac Implants 2013;28:1261–1271.
26. Funato A, Ogawa T. Photofunctionalized dental implants: A case series in compromised bone. Int J Oral Maxillofac Implants 2013; 28:1589–1601.
27. Suzuki S, Kobayashi H, Ogawa T. Implant stability change and osseointegration speed of immediately loaded photofunctionalized implants. Implant Dent 2013;22:481–490.
28. Pyo SW, Park YB, Moon HS, Lee JH, Ogawa T. Photofunctionalization enhances bone-implant contact, dynamics of interfacial osteogenesis, marginal bone seal, and removal torque value of implants: A dog jawbone study. Implant Dent 2013;22:666–675.
29. Ueno T, Yamada M, Hori N, Suzuki T, Ogawa T. Effect of ultraviolet photoactivation of titanium on osseointegration in a rat model. Int J Oral Maxillofac Implants 2010;25:287–294.
30. Takeuchi K, Saruwatari L, Nakamura HK, Yang JM, Ogawa T. Enhanced intrinsic biomechanical properties of osteoblastic mineralized tissue on roughened titanium surface. J Biomed Mater Res A 2005;72A:296–305.
31. Ogawa T, Ozawa S, Shih JH, et al. Biomechanical evaluation of osseous implants having different surface topographies in rats. J Dent Res 2000;79:1857–1863.
32. Ogawa T, Nishimura I. Different bone integration profiles of turned and acid-etched implants associated with modulated expression of extracellular matrix genes. Int J Oral Maxillofac Implants 2003;18:200–210.
33. Ikeda T, Hagiwara Y, Hirota M, et al. Effect of photofunctionalization on fluoride-treated nanofeatured titanium. J Biomater Appl 2014;28:1200–1212.
34. Butz F, Ogawa T, Chang TL, Nishimura I. Three-dimensional bone-implant integration profiling using micro-computed tomography. Int J Oral Maxillofac Implants 2006;21:687–695.
35. Tsukimura N, Yamada M, Aita H, et al. N-acetyl cysteine (NAC)-mediated detoxification and functionalization of poly(methyl methacrylate) bone cement. Biomaterials 2009;30:3378–3389.
36. Klinger A, Steinberg D, Kohavi D, Sela MN. Mechanism of adsorption of human albumin to titanium in vitro. J Biomed Mater Res 1997; 36:387–392.
37. Ellingsen JE. A study on the mechanism of protein adsorption to TiO2. Biomaterials 1991;12:593–596.
38. Stein GS, Lian JB. Molecular mechanisms mediating proliferation/differentiation interrelationships during progressive development of the osteoblast phenotype. Endocr Rev 1993;14:424–442.
39. Siddhanti SR, Quarles LD. Molecular to pharmacologic control of osteoblast proliferation and differentiation. J Cell Biochem 1994;55:310–320.
40. Alborzi A, Mac K, Glackin CA, Murray SS, Zernik JH. Endochondral and intramembranous fetal bone development: Osteoblastic cell proliferation, and expression of alkaline phosphatase, m-twist, and histone H4. J Craniofac Genet Dev Biol 1996;16:94–106.
41. Owen TA, Aronow M, Shalhoub V, et al. Progressive development of the rat osteoblast phenotype in vitro: Reciprocal relationships in expression of genes associated with osteoblast proliferation and differentiation during formation of the bone extracellular matrix. J Cell Physiol 1990;143:420–430.